JM PAPERS

Effects of horizontal magnetic fields on turbulent Rayleigh–Bénard convection in a cuboid vessel with aspect ratio $\Gamma = 5$

Long Chen[1], Zhao-Bo Wang[1] and Ming-Jiu Ni[1],†

[1]School of Engineering Science, University of Chinese Academy of Sciences, Beijing 101408, PR China

Direct numerical simulations have been conducted to investigate turbulent Rayleigh–Bénard convection (RBC) of liquid metal in a cuboid vessel with aspect ratio $\Gamma = 5$ under an imposed horizontal magnetic field. Flows with Prandtl number $Pr = 0.033$, Rayleigh numbers ranging up to $Ra \leq 10^7$, and Chandrasekhar numbers up to $Q \leq 9 \times 10^6$ are considered. For weak magnetic fields, our findings reveal that a previously undiscovered decreasing region precedes the enhancement of heat transfer and kinetic energy. For moderate magnetic fields, we have reproduced the reversals of the large-scale flow, which are considered a reorganization process of the roll-like structures that were reported experimentally by Yanagisawa *et al.* (*Phys. Rev.* E, vol. 83, 2011, 036307). Nevertheless, the proposed approach of skewed-varicose instability has been substantiated as insufficient to elucidate fundamentally the phenomenon of flow reversal, an occurrence bearing a striking resemblance to the large-scale intermittency observed in magnetic channel flows. As we increase the magnetic field strength further, we observe that the energy dissipation of the system comes primarily from the viscous dissipation within the boundary layer. Consequently, the dependence of Reynolds number Re on Q approaches a scaling as $Re\,Pr/Ra^{2/3} \sim Q^{-1/3}$. At the same time, we find the law for the cutoff frequency that separates large quasi-two-dimensional scales from small three-dimensional ones in RBC flow, which scales with the interaction parameter as $\sim N^{1/3}$.

Key words: Bénard convection, MHD turbulence

1. Introduction

The investigation into the nature of thermal convection under the influence of magnetic fields has been invoked frequently to explore the fundamental principles of magnetoconvection, owing to its broad range of applications, including stable crystal

† Email address for correspondence: mjni@ucas.ac.cn

growth and the optimization of heat exchanger performance (Busse & Clever 1983; Cioni, Chaumat & Sommeria 2000; Tasaka *et al.* 2016; Liu, Krasnov & Schumacher 2018; Akhmedagaev *et al.* 2020*a*; Vogt *et al.* 2021). Unlike regular fluids, flowing liquid metal under the influence of a magnetic field generates induced currents and interacts with the magnetic field to produce Lorentz force, thereby altering its original motion characteristics. Normally, due to the low viscosity of liquid metals, they tend to develop into turbulence quite easily. When a magnetic field is applied, the flow becomes anisotropic and even two-dimensional (2-D) as it stretches along the direction of the field. However, the influence of the magnetic field can manifest itself in different ways (Eckert *et al.* 2001; Pothérat & Klein 2017).

One classical model for studying the impact of magnetic fields on thermal convection systems driven by temperature differences is Rayleigh–Bénard convection (RBC). This system is deceptively simple. Electrically conducting fluid confined in a cuboid vessel is exposed to a horizontal magnetic field, and a destabilizing vertical temperature gradient is heated from the bottom and cooled from the top. There are three important dimensionless control parameters in such a system: the Rayleigh number, Chandrasekhar number and Prandtl number, which are given by

$$Ra = \frac{g\alpha \, \Delta T \, H^3}{\nu\kappa}, \quad Q = B_0^2 L^2 \frac{\sigma}{\rho\nu} \quad \text{and} \quad Pr = \frac{\nu}{\kappa}, \quad (1.1a\text{--}c)$$

with the gravity acceleration g, the thermal expansion coefficient α, the temperature difference between the horizontal boundaries of the fluid layer ΔT, the height of the layer H, the kinematic viscosity ν, the temperature diffusivity κ, the electrical conductivity σ, the mass density ρ, and the imposed magnetic field strength B_0. The cuboid vessel has a square cross-section with horizontal side lengths L and aspect ratio $\Gamma = L/H$.

For a much smaller Prandtl number flow, the transition from steady convection to turbulence occurs more drastically with increasing Ra (Krishnamurti & Howard 1981) and gives rise to much smaller stable regions of 2-D convection rolls in RBC. Through a stability analysis, Busse (1978) showed that the stable convection rolls region, also called the 'Busse balloon', shrinks with decreasing Pr, which makes it difficult to be realized in experiments at low Pr conditions. Nonetheless, invariably the implementation of a horizontal magnetic field is employed to surmount the aforesaid predicament. For instance, the weakly nonlinear theory postulates that magnetic fields having a diminutive Q expand the Busse balloon region, as proposed by Busse & Clever (1983) regarding stability concerns. In other words, when Ra is sufficiently high, convection rolls will become unstable, undergo transition, and exhibit a plethora of intriguing flow phenomena such as turbulence as the magnetic field decreases gradually. The research conducted by Houchens, Witkowski & Walker (2002) indicates that for RBC, increasing the vertical magnetic field strength leads to an increase in the critical Ra at which instability occurs.

Regarding the impact of horizontal magnetic fields on thermal convection, the essential aspect lies in the constraint imposed by the wall, such as Hartmann braking. Burr & Müller (2002) characterized this effect as the increasing of the onset convection threshold, and predicted an increase in the wavenumber of 2-D rolls with the rise of Q. Additionally, they demonstrated further the occurrence of turbulent thermal convection induced by oscillatory convection through the adjustment (Ra, Q). The evidence of turbulent thermal convection being suppressed by an increase in Q for a fixed Ra is substantiated by variations in the power spectrum of temperature fluctuations within the fluid layer. Nevertheless, these variations do not depict a straightforward progression

towards turbulent thermal convection, leaving some intricate flow structures unexplained due to the limited information on the flow field.

Recently, with the development of ultrasonic velocity measurement, statistical spatio-temporal convection patterns in a liquid metal have been studied experimentally, and various flow regimes and transitions between them have been uncovered (Yanagisawa *et al.* 2011, 2013; Yanagisawa, Hamano & Sakuraba 2015; Tasaka *et al.* 2016; Vogt *et al.* 2018, 2021). Yanagisawa *et al.* (2011) conducted numerous experiments on heat transfer in the presence of a horizontal magnetic field, and summarized multiple complex flow mechanisms. For instance, in a flat container with aspect ratio 5, they observed stable four-roll and four-roll reversal phenomena as the horizontal magnetic field increased, and they measured the frequency of the reversal. Subsequently, Yanagisawa *et al.* (2013) increased the values of *Ra* and *Q*, and summarized various flow mechanisms within the given parameter space, including no-roll, the transition from four-roll to three-roll, four-roll oscillation, the transition from five-roll to four-roll, stable five-roll, stable four-roll, and no convection. To gain deeper insight into the mechanism of flow reversal, Yanagisawa *et al.* (2015) provided a detailed description of the reversal process and attempted to explain it in terms of skewed-varicose instability. Vogt *et al.* (2018) also believed that this flow reversal might be caused by oscillation instability and skewed-varicose instability, but there is still no definitive mechanism to explain this conversion process. At the same time, Vogt *et al.* (2018) cleverly designed a set of experiments that depicted the evolution of flow from stable to unstable, from two to three dimensions, by fixing *Ra* and gradually reducing *Q*. Consequently, they obtained typical flow mechanisms similar to those discovered by Yanagisawa *et al.* (2013), and also focused on secondary flow in the Hartmann layer in parallel and perpendicular magnetic field directions. Subsequently, Vogt *et al.* (2021) and Yang, Vogt & Eckert (2021) conducted similar experiments and discovered that the magnetic field resulted in a significant enhancement of heat and momentum transport. However, there is a lack of mechanistic explanation for the scales relevant to the convective flow and heat transfer.

The focus of our investigation here is on the RBC with a horizontal magnetic field and sidewalls. High-resolution direct numerical simulations (DNS) of flows in a cuboid vessel with $\Gamma = 5$, $Pr = 0.033$, $10^5 \leq Ra \leq 10^7$ and $Q \leq 9 \times 10^6$ are performed. The work follows the experiments by Yang *et al.* (2021) carried out at the same Γ and Pr, and at $Ra \leq 2.6 \times 10^5$ and $Q \leq 6.1009 \times 10^6$ (the highest *Ra* and *Q* achieved so far). The work aims to answer the following general questions.

(i) How do the flow structures in the convection cavity change under the influence of a horizontal magnetic field? Additionally, what is the impact of these structures on turbulent heat and momentum transport?

(ii) Under the influence of a magnetic field, is the skewed-varicose instability the intrinsic mechanism driving the phenomenon of reversed flow in a multiple roll system of Yang *et al.* (2021) and Vogt *et al.* (2021)?

(iii) According to the findings of Vogt *et al.* (2018), it is evident that with the enhancement of the magnetic field, the flow in the RBC thermal convection problem undergoes a transition from three dimensions to two as well. Therefore, is there also a cutoff frequency or length scale between quasi-2-D and three-dimensional (3-D) flow structures in magnetohydrodynamics (MHD) RBC turbulence, as predicted by Sommeria & Moreau (1982) and found by Baker *et al.* (2018) and Chen *et al.* (2021) in MHD channel flows? And what kind of relationship exists between the cutoff frequency and the interaction parameter?

To the best of our knowledge, this study is the first to analyse turbulent RBC at high Q, realistically low Pr, and a large aspect ratio $\Gamma = 5$ in the framework of high-resolution DNS. The only related simulations have been performed by Lim *et al.* (2019) in a cubic convection cell at unrealistic $Pr = 8$, with Ra up to 10^{10}, and Q up to 6.4×10^5, and by Akhmedagaev *et al.* (2020*b*) in a cylindrical cavity with $\Gamma = 1$ at $Pr = 0.025$, with Ra up to 10^9, and Q up to 1.96×10^6, where axial magnetic fields are imposed.

2. Problem statement and formulation

We consider the flow of an incompressible, viscous, electrically conducting fluid (a liquid metal) with constant physical properties contained in a square vessel under a uniform horizontal magnetic field. The governing equations are made dimensionless by using the vessel's height H, the free-fall velocity $U = \sqrt{g\alpha\,\Delta T\,H}$, the external magnetic field strength B_0, and the imposed temperature difference $\Delta T = T_{bottom} - T_{top}$ as the scales of length, velocity, magnetic field and temperature, respectively. The Boussinesq and quasi-static approximations are used. The equations are

$$\nabla \cdot \boldsymbol{u} = 0, \tag{2.1}$$

$$\frac{\partial \boldsymbol{u}}{\partial t} + (\boldsymbol{u} \cdot \nabla)\boldsymbol{u} = -\nabla p + \sqrt{\frac{Pr}{Ra}}\left(\nabla^2 \boldsymbol{u} + \frac{Q}{\Gamma^2}\,(\boldsymbol{j} \times \boldsymbol{e}_b)\right) + T\boldsymbol{e}_z, \tag{2.2}$$

$$\frac{\partial T}{\partial t} + \boldsymbol{u} \cdot \nabla T = \frac{1}{\sqrt{Ra\,Pr}}\,\nabla^2 T, \tag{2.3}$$

$$\boldsymbol{j} = -\nabla\phi + (\boldsymbol{u} \times \boldsymbol{e}_b), \tag{2.4}$$

$$\nabla^2\phi = \nabla \cdot (\boldsymbol{u} \times \boldsymbol{e}_b), \tag{2.5}$$

where p, $\boldsymbol{u}$, ϕ and T are the fields of pressure, velocity, electric potential and deviation of temperature from a reference value, and $\boldsymbol{e}_b$ is the unit vector in the direction of the imposed magnetic field $\boldsymbol{B}_0$. In the present study, the magnetic fields are paralleled with y-axial direction. The top and bottom walls are maintained at constant temperatures $T = -0.5$ and $T = 0.5$, respectively. The lateral walls are thermally insulated, so having $\partial T/\partial n = 0$. No-slip boundary conditions for velocity are applied at the walls. All walls are perfectly electrically insulated, which implies $\partial\phi/\partial n = 0$.

The governing equations (2.1)–(2.5) are solved numerically using a second-order finite volume method on a non-uniform Cartesian mesh, discussed in detail in Chen *et al.* (2021). Table 1 summarizes the most important parameters of our DNS runs, and reports the (turbulent) momentum transfer quantified by the Reynolds number $Re = u_{rms}\sqrt{Ra/Pr}$ with root mean square velocity $u_{rms} = \sqrt{\langle u_x^2 + u_y^2 + u_z^2 \rangle_{V,t}}$ and (turbulent) heat transfer measured by the Nusselt number $Nu = 1 + \sqrt{Ra\,Pr}\,\langle u_z T \rangle_{V,t}$, where $\langle\cdot\rangle_{V,t}$ stands for volume and time averaging, respectively. The time averaging is performed over 40 convective time units. The values of Re and Nu of run 1 are comparable to those from Liu *et al.* (2018) for RBC in mercury at $Pr = 0.025$ in a closed square cell at $\Gamma = 4$, where $Nu = 9.75 \pm 0.05$ and $Re = 7946 \pm 19$ are reported. We find that grids with $N_x \times N_y \times N_z = 1536 \times 1536 \times 384$, and the points inside the boundary layers, are sufficient for non-magnetic/magnetic flows. Further refinement of the grid does not lead to significant changes. In addition, suppression of velocity gradients by the magnetic field allows us to alleviate the resolution requirements for the x, z directions.

Run	Ra	Q	$N_x \times N_y \times N_z$	Nu	Re	N_{BL}	Runtime
1	10^7	0	$1280 \times 1280 \times 256$	9.26 ± 0.05	7755 ± 21	14	40
2	10^7	0	$1536 \times 1536 \times 384$	9.30 ± 0.03	7764 ± 17	16	40
3	10^7	0	$1920 \times 1920 \times 384$	9.31 ± 0.03	7765 ± 17	20	40
4	10^7	2.25×10^6	$1280 \times 1280 \times 256$	11.61 ± 0.05	$10\,435 \pm 14$	10	40
5	10^7	2.25×10^6	$1536 \times 1536 \times 384$	11.75 ± 0.02	$10\,447 \pm 8$	12	40
6	10^7	2.25×10^6	$1920 \times 1920 \times 384$	11.76 ± 0.02	$10\,447 \pm 8$	14	40

Table 1. The grid sensitivity study for cases with $Pr = 0.033$, $Ra = 10^7$ and $\Gamma = 5$. The grid number inside the Hartmann layer with thickness δ_{Ha} is listed. For the case $Q = 0$, the viscous boundary layer thickness δ_v is adopted instead of the Hartmann layer thickness. We use N_{BL} to denote the number of the grid points within the boundary layer. The total runtime is scaled with the free-fall time, $t_f = H/U_f$.

In addition to the internal structure of the flow, four boundary layers need to be resolved accurately (Grossmann & Lohse 2001; Davidson 2002): the thermal boundary layer of thickness $\delta_T \approx 1/(2Nu)$, the viscous boundary layer with $\delta_v \approx 1/(4\sqrt{Re})$, the Shercliff layer with $\delta_{Sh} \approx 1/\sqrt[4]{Q}$ at the lateral, top and bottom walls, and the Hartmann layer with $\delta_{Ha} = 1/\sqrt{Q}$ at the walls perpendicular to the magnetic field. Therefore, coordinate transformation is applied for generation of a non-uniform grid (see Akhmedagaev *et al.* 2020*a*). In the present simulation, grids $512 \times 512 \times 128$, $1024 \times 1024 \times 256$, $1536 \times 1536 \times 384$, and the clustering parameter 2.0 (Akhmedagaev *et al.* 2020*b*) are applied for flows with $Q \leq 9 \times 10^4$ at $Ra = 10^5$, 10^6 and 10^7, respectively. When the magnetic field is relatively strong, $Q > 9 \times 10^4$, taking into account the quasi-2-D character of the MHD flow (i.e. weak axial gradients of velocity in the core), we appropriately reduce the grid points in the direction of the magnetic field (but not less than 4/5 of the original number), and the grid points in the Hartmann layer are no less than 10.

3. Results and discussion

3.1. *Global heat and mass transfer*

With the increasing of magnetic field imposed on RBC, the electromagnetic force gives rise to a transition from a 3-D convective roll pattern (called cell structures by Vogt *et al.* (2021); see figure 1*a*) to a quasi-2-D flow pattern (see figure 1*d*) in a way that convective rolls become more and more aligned with the magnetic field (see figures 1*b*,*c*). Such an evolution has been observed already in the previous investigations by Burr & Müller (2002), Tasaka *et al.* (2016) and Vogt *et al.* (2021). Generally speaking, the quasi 2-D roll-like structure ensures a direct heat transfer between the bottom and the top, and extends the uniform bulk central region of the convection, thinning the thermal boundary layers and causing an increase of heat transfer coefficient for moderate Q as shown in figure 2(*a*).

However, prior to the augmentation of heat transfer, it is noteworthy that Nu exhibits a decline under relatively weak magnetic fields, particularly in cases of higher Ra, which is consistent with the findings of the experiments conducted by Burr & Müller (2002) and Vogt *et al.* (2021). The reduction can be attributed to the suppression of small-scale convective vortices by the Lorentz force, which results in a decrease in the injection of plumes, the primary agents of heat transfer. It is also important to mention that Re follows a similar trend to the Nusselt number with the increase of Q, indicating that convective heat conduction is always dominant within our parameter space. Moreover, this trend
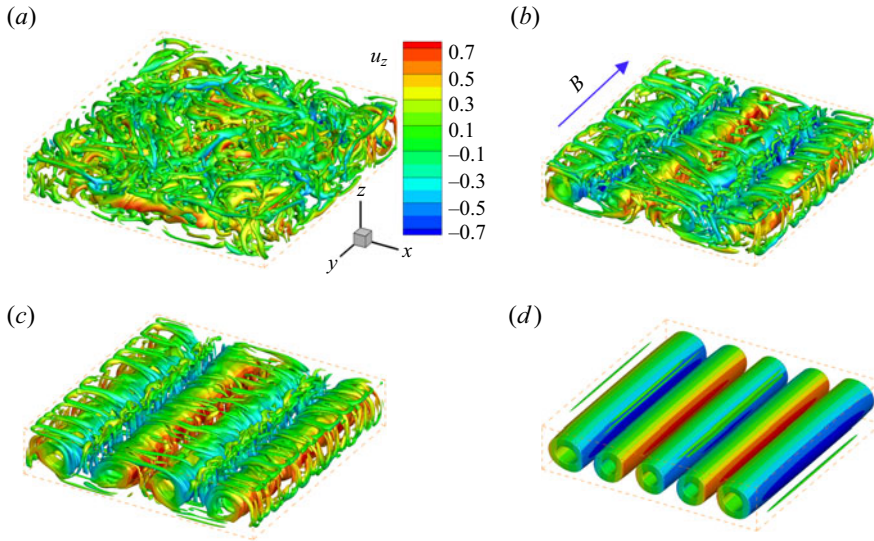
Figure 1. The isosurfaces of $\Omega = 0.5$ are shown, coloured with vertical velocity u_z for $Ra = 1 \times 10^6$. The identified method of the vortex structures (Ω) applied here is defined by Liu *et al.* (2016). Isosurfaces are for (*a*) $Q/Ra = 0$, (*b*) $Q/Ra = 0.16$, (*c*) $Q/Ra = 0.64$, and (*d*) $Q/Ra = 2.25$.
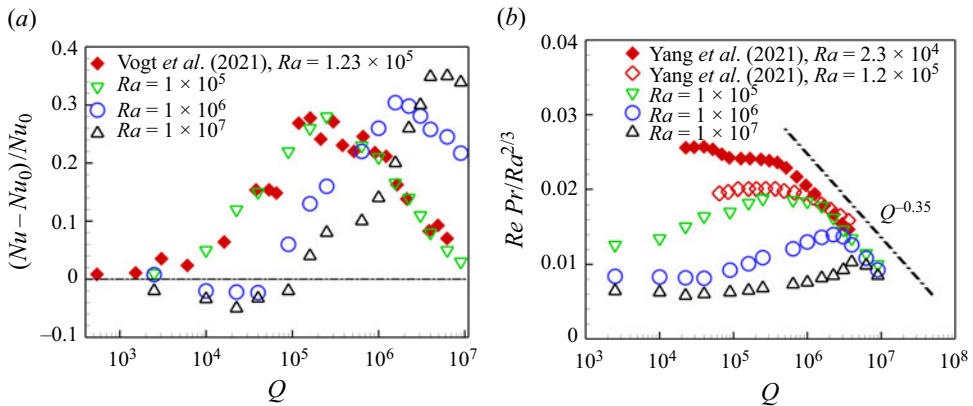

Figure 2. (*a*) Relative deviations of the heat transfer from the reference state of RBC (without magnetic field), $(Nu - Nu_0)/Nu_0$, as a function of Q for three different Ra values. Data from Vogt *et al.* (2021) are used for comparison. (*b*) The corresponding values of the compensated Re number, $Re\,Pr/Ra^{2/3}$, plotted versus Q, where Re from Yang *et al.* (2021) is based on $\max(u_x)$. The Q values in the simulation are listed in ascending order as follows: 2.5×10^3, 10^4, 2.25×10^4, 4×10^4, 9×10^4, 1.6×10^5, 2.5×10^5, 6.4×10^5, 10^6, 1.5625×10^6, 2.25×10^6, 3.0625×10^6, 4×10^6, 6.25×10^6 and 9×10^6.

exhibits the intricate way in which a magnetic field affects a turbulent flow. For small Q, the velocity in the magnetic field is inhibited, and damping becomes the primary effect on flow, resulting in a decrease in Re. However, for moderate Q, the enhancement of flow perpendicular to the magnetic field dominates, leading to an increase in both Nu and Re. This phenomenon has also been observed in duct flow (Sukoriansky, Zilberman & Branover 1986; Zikanov *et al.* 2019), electromagnetically driven square cavity flow (Pothérat & Klein 2017) and vertical convection flow in a square container under the influence of magnetic fields (Chen, Liu & Ni 2018).

980 A24-6

Furthermore, we note that $Re\,Pr/Ra^{2/3}$ scales well with Q^{-n} ($n = 0.35$) for cases at sufficiently large Q, where quasi-2-D roll structures have been well developed. Now we incorporate Grossmann–Lohse (GL) theory (Grossmann & Lohse 2000) into the MHD-RBC flow, and provide an explanation for this scaling relationship. Regarding a regular flow, the GL theory takes into account the spatial- and time-averaged viscous and thermal dissipation rates, ε_ν and ε_κ, in convective heat transfer:

$$\varepsilon_\nu = \frac{\nu}{2}\,\langle(\partial_i u_j + \partial_j u_i)^2\rangle, \tag{3.1}$$

$$\varepsilon_\kappa = \kappa\,\langle(\partial_i T)^2\rangle. \tag{3.2}$$

Here, the Einstein summation convention is used over the coordinates $i, j = x, y, z$, and $\partial_i = \partial/\partial x_i$ is a short notation for the spatial partial derivatives.

As suggested by Zürner (2020), under the influence of a magnetic field, the additional Joule dissipation rate

$$\varepsilon_\eta = \frac{\eta}{2}\,\langle(\partial_i b_j + \partial_j b_i)^2\rangle \tag{3.3}$$

has to be considered. Here, the secondary magnetic field $\boldsymbol{b} = b_i \boldsymbol{e}_i$ is induced by the interaction of $\boldsymbol{u}$ and the imposed magnetic field $\boldsymbol{B}_0$, and η is the the magnetic diffusivity. When turbulence reaches a relatively steady state, the average dissipation rate satisfies the following rigorous relations, which are derivable easily from (2.2), (2.3), the transport equation for magnetic induction, and the definition of Nu (see Shraiman & Siggia 1990; Chakraborty 2008; Zürner *et al.* 2016):

$$\varepsilon_\nu + \frac{\varepsilon_\eta}{\mu\rho_0} = \frac{\nu^3}{H^4}\frac{(Nu - 1)\,Ra}{Pr^2}, \tag{3.4}$$

$$\varepsilon_\kappa = \kappa\frac{(\Delta T)^2}{H^2}\,Nu, \tag{3.5}$$

where μ represents the the magnetic permeability. Based on the GL theory, the contributions of the dissipation rate from the bulk region and the boundary layer are separated:

$$\varepsilon_\nu = \varepsilon_{\nu,Bulk} + \varepsilon_{\nu,BL}, \tag{3.6}$$

$$\varepsilon_\eta = \varepsilon_{\eta,Bulk} + \varepsilon_{\eta,BL}, \tag{3.7}$$

$$\varepsilon_\kappa = \kappa\frac{(\Delta T)^2}{H^2} + \varepsilon_{\kappa,Bulk} + \varepsilon_{\kappa,BL}. \tag{3.8}$$

Zürner (2020) made estimates for the different terms in the above equations, based on the following assumptions: (1) the Prandtl number of liquid metals is sufficiently low, $Pr \ll 1$; (2) $Q^{1/2}$ is sufficiently large, and the viscous boundary layers on the walls perpendicular to the magnetic fields are replaced by the Hartmann layer; (3) the magnetic Reynolds number is low enough, $Rm \ll 1$; and (4) additional regime transitions, e.g. transition concerning the onset of convection under the effects of magnetic fields. He obtained the following

N	75.60	174.69	253.46	530.34	1045.96
$\varepsilon_{v,Bulk}$	0.0101	0.0133	0.0149	0.0188	0.0161
$\varepsilon_{v,BL}$	0.0359	0.0587	0.0768	0.1620	0.1395
$\varepsilon_{\eta,Bulk}$	0.0333	0.0173	0.0137	0.0021	0.0012
$\varepsilon_{\eta,BL}$	0.0212	0.0177	0.0139	0.0092	0.0085
N_{roll}	3	4	4	5	5

Table 2. Comparison of the volume- and time-averaged viscous dissipation ε_v, the Joule dissipation rates ε_η, and the averaged number of the roll structures at $Ra = 1 \times 10^6$.

relationships:

$$\varepsilon_{v,Bulk} \sim \frac{v^3}{H^4} Re^3, \tag{3.9}$$

$$\varepsilon_{v,BL} \sim \frac{v^3}{H^4} Re^2 Q^{1/2}, \tag{3.10}$$

$$\varepsilon_{\eta,Bulk} \sim \mu\rho_0 \frac{v^3}{H^4} Re^2 Q, \tag{3.11}$$

$$\varepsilon_{\eta,BL} \sim \mu\rho_0 \frac{v^3}{H^4} Re^2 Q^{3/2}, \tag{3.12}$$

$$\varepsilon_{\kappa,Bulk} \sim \kappa \frac{(\Delta T)^2}{H^2} Re\,Pr, \tag{3.13}$$

$$\varepsilon_{\kappa,BL} \sim \kappa \frac{(\Delta T)^2}{H^2} \sqrt{Re\,Pr}. \tag{3.14}$$

When $N\ (= Q/Re)$ is large enough, the bulk flow region approaches a quasi-2-D state, where the viscous dissipation should be dominated by $\varepsilon_{v,BL}$. To substantiate this viewpoint more rigorously, we have tabulated the time-averaged values of viscous and Joule dissipation in the bulk flow and boundary layer regions, respectively, when $Ra = 1 \times 10^6$, as shown in table 2. It is worth noting that when considering dissipation, especially in the bulk flow region, forces other than the Lorentz force, such as the inertial force, must also be taken into account (Pothérat & Klein 2017). Therefore, N is used as a control parameter here. The results demonstrate strongly that when $N \geq 253.46$, the viscous dissipation in the bulk flow region is much smaller than that in the boundary layer, almost $\varepsilon_{v,Bulk} \approx 0.1\varepsilon_{v,BL}$. Therefore, it can be concluded that the main contribution to viscous dissipation comes from the boundary layer, i.e. $\varepsilon_v \sim \varepsilon_{v,BL}$. This approximation is evidently unsuitable for cases where N is relatively small. For instance, when $N = 75.60$, the viscous dissipation in the bulk flow region is similar to that in the boundary layer. Meanwhile, the thermal dissipation for convective liquid metals with $Pr \ll 1$ satisfies $\varepsilon_\kappa \sim \varepsilon_{\kappa,BL}$.

For the Joule dissipation, when the magnetic field is strong enough, it can be inferred from (3.11) and (3.12) that the contribution from the boundary layer should be greater than that from the bulk region. This phenomenon can be explained easily from a physical perspective. Under a strong magnetic field, the flow becomes more regular, and the Joule dissipation in the bulk region is small. The electric current concentrates mainly in the Hartmann layer, thus resulting in greater Joule dissipation in the boundary layer.

The computational results also confirm this viewpoint. When the magnetic field is weak, such as $N = 75.60$, 174.69 and 253.46, the Joule dissipation in the bulk region is roughly equivalent to that in the boundary layer. However, as the magnetic field continues to increase and N reaches 530.34 and 1045.96, the Joule dissipation in the bulk region is significantly lower than that in the boundary layer.

It is difficult to obtain the relative magnitudes of viscous dissipation and Joule dissipation from the approximate equations (3.9)–(3.12) under a strong magnetic field. Based on the calculation results, it can be observed that when the magnetic field is weak, such as $N < 253.46$, the contributions of viscous dissipation and Joule dissipation are relatively close. When $N \geq 253.46$, viscous dissipation will be much greater than Joule dissipation, and as the magnetic field continues to increase, the difference between the two will become more significant. Therefore, under a strong magnetic field, we can conclude that

$$\varepsilon_\nu + \varepsilon_\eta \sim \varepsilon_\nu \sim \varepsilon_{\nu,BL}. \tag{3.15}$$

From this, it can be derived that the momentum dissipation (including both the viscous dissipation and Joule dissipation) and thermal dissipation for $Pr \ll 1$ (Grossmann & Lohse 2000) satisfy approximately

$$\frac{(Nu - 1)\,Ra}{Pr^2} \sim Re^2\,Q^{1/2}, \tag{3.16}$$

$$Nu - 1 \sim \sqrt{Re\,Pr}. \tag{3.17}$$

Regarding the flow of liquid metal studied in this paper, with Pr being unchanged, it can be obtained that

$$(\sqrt{Re\,Pr})Ra \sim Re^2\,Q^{1/2} \rightarrow Re\,Pr/Ra^{2/3} \sim Q^{-1/3}. \tag{3.18}$$

As shown in figure 2(*b*), the numerical results exhibit a scaling law of 0.35 for cases at different Ra, which agrees well with the derived scaling law of $1/3$.

3.2. *Flow reversal and turbulence intermittency*

The phenomenon of flow reversal, which was observed previously in experimental studies at $Ra \sim 10^5$ (Yanagisawa *et al.* 2011, 2013) and numerical studies at $Ra \leq 10^6$ (Vogt *et al.* 2018; Liu 2019), has been rediscovered in the present work at $Ra = 10^7$ with a larger aspect ratio $\Gamma = 5$. Our investigations have revealed that this reversal phenomenon is an inherent characteristic of MHD-RBC flows, and is associated with specific parameter combinations. Furthermore, we intend to provide a detailed depiction of the evolution process of flow reversals based on the integrated kinetic energy equation

$$\frac{\mathrm{d}}{\mathrm{d}t} \int \frac{u^2}{2}\,\mathrm{d}V = -\int \varepsilon_\nu\,\mathrm{d}V - \int \varepsilon_\eta\,\mathrm{d}V + \int u_z T\,\mathrm{d}V, \tag{3.19}$$

where V represents the entire domain. Presented here are the developments in the flow field resulting from a singular flow reversal procedure, as well as the subsequent evolutions of the kinetic energy u^2, with regard to u_x^2, u_y^2 and u_z^2, the rate of viscous dissipation ε_ν, the rate of Joule dissipation ε_η, and the thermal flux $u_z T$.

The exemplification of temporal progression manifests in figures 3 and 4, where turbulent bursts alternate with periods of quasi-2-D behaviour. As delineated in figure 4(*a*), the nascent phase (t_1) manifests as quasi-2-D, comprising four quasi-2-D rolls labelled as
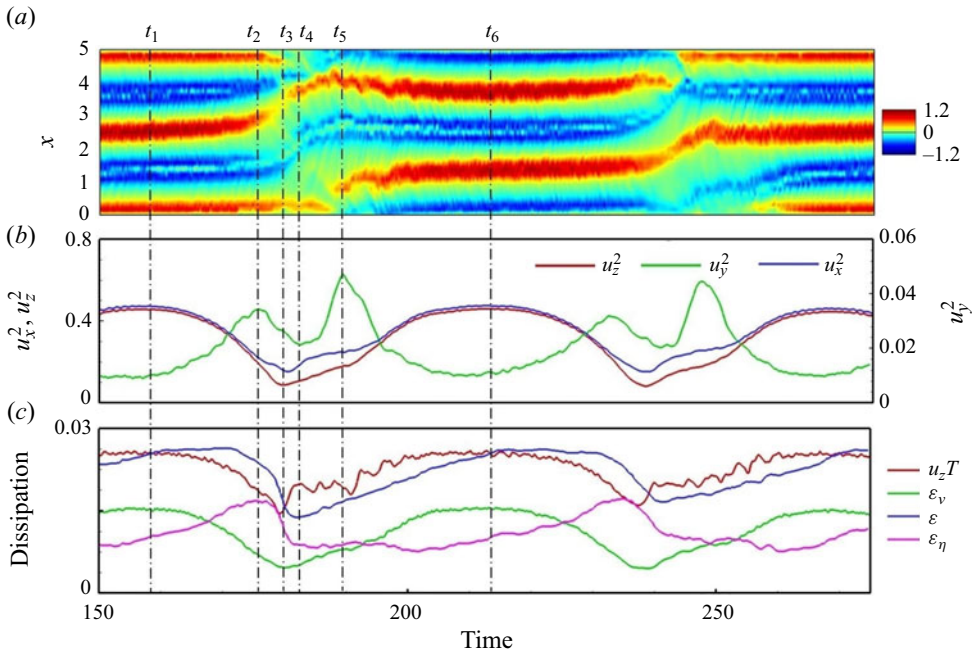
Figure 3. Results for $Q = 2.25 \times 10^6$, $Ra = 1 \times 10^7$. (*a*) Time-space maps of vertical velocity along line (2.5, *y*, 0.75). (*b*) Time variations of energy u_x^2, u_y^2, u_z^2. (*c*) Time variations of the volume-averaged heat transport $u_z T$, viscous dissipation rate ε_ν, and Joule dissipation rate ε_η.
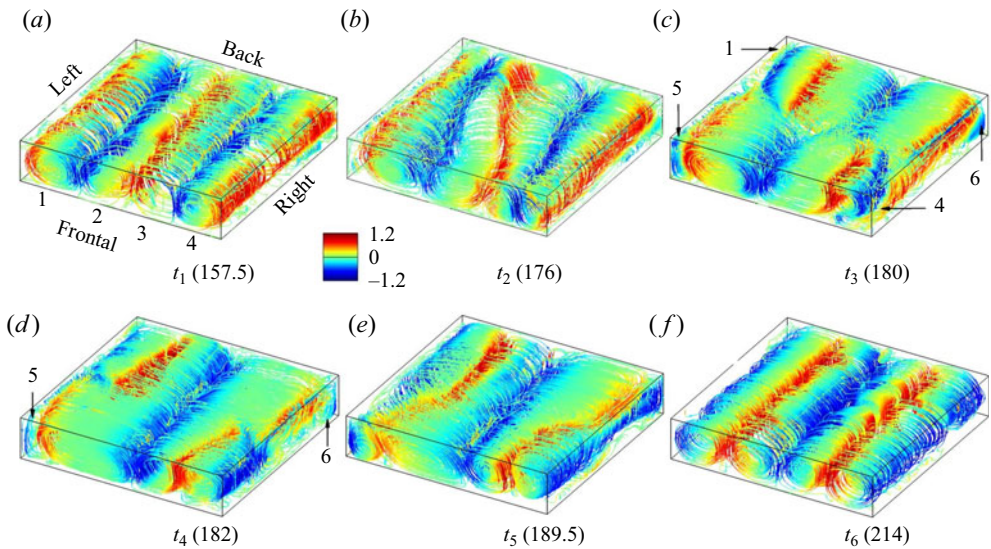

Figure 4. Flow evolution during one reversal procedure with $Q = 2.25 \times 10^6$, $Ra = 1 \times 10^7$. Six snapshots are shown, denoted by the six vertical dashed lines in figure 3. The streamlines of 3-D velocity field are coloured with vertical velocity: red for upwards motion, and blue for downwards motion.

1, 2, 3 and 4, correspondingly. At this juncture, the vertical energy diminishes substantially but does not reach null, while the energy within the plane perpendicular to the magnetic field attains its zenith, illustrated in figure 3(*c*). Progressing from time t_1 to t_2, the rolls undergo curvature where the latter halves of rolls 1 and 2 contract, whereas rolls 3 and

4 expand, exhibiting an evolution contrary to that near the frontal wall. Throughout this process, depicted in figure 3, both u_y^2 and the Joule dissipation ε_η escalate, reaching their peak at t_2, signifying that the restoration of 3-D turbulent flow occurs. Following this, from t_2 to t_3, as the rolls persist in their curvature, rolls 5 and 6 materialize at the extremities of the vessel, as portrayed in figure 4(*c*), while the roll-like configurations adjacent to the remaining corners almost dissipate. Concurrently, rolls 2 and 3 undergo displacement in the centre (refer to figure 4). During this phase, u_y^2 declines, and the predominant contributions of kinetic energy, u_x^2 and u_z^2, also dwindle further as $\varepsilon_\nu + \varepsilon_\eta$ continues to surpass $u_z T$. When the intersection of $\varepsilon_\nu + \varepsilon_\eta$ with $u_z T$ occurs at t_3, u_x^2 and u_z^2 attain their minimum values.

From the interval between t_3 and t_5, the fragmented convection rolls begin a process of reintegration. Roll 5, newly formed, inclines towards the posterior section of roll 2, while the leading half of roll 3 appears to merge with the recently generated roll 6. Within the central zone, the trailing half of roll 3 endeavours to connect with the leading half of roll 1, while the frontal section of roll 2 seeks to bond with the rear part of roll 4. Throughout this phase, the magnitude of $u_z T$ surpasses that of $\varepsilon_\nu + \varepsilon_\eta$, consequently initiating an ascent in both u_x^2 and u_z^2. As alignment between the rolls and the magnetic field occurs at t_4, the values of u_y^2 and $\varepsilon_\nu + \varepsilon_\eta$ descend to their minimal levels. By t_6, $\varepsilon_\nu + \varepsilon_\eta$ exceeds $u_z T$, leading to a surge in u_x^2 and u_z^2. A novel quasi-2-D structure emerges, comprising four rolls rotating in the opposite direction to those observed at t_1.

Let us now examine the possible physical mechanisms of flow reversal, i.e. the skewed-varicose instability. As mentioned by Greenside, Cross & Coughran (1988) and Busse, Kropp & Zaks (1992), the skewed-varicose instability is crucial for understanding the transition of fluid from small to medium Pr ($Pr \leq 1$) towards chaos. One of its key elements is the mean flow, which refers to the flow with a larger length scale compared to the wavelength of convective eddies. Yanagisawa *et al.* (2013, 2015) and Vogt *et al.* (2018) explained the process of flow reversals in RBC as the creation of new rolls and the following skewed-varicose instability (instability in both directions perpendicular and parallel to the axis of roll). In this process, the horizontal circulation plays an important role, which can be quantified by introducing the global angular momentum. For our research, the global angular momentum along the z direction around the centre point $C(x_c, y_c, z_c)$ of the container can well reflect the mean flow. This is defined as $L(z) = \langle (x - x_c)u_y - (y - y_c)u_x \rangle_V$, where the brackets denote the spatial average.

Upon examining figure 5, it is apparent that under the condition $Ra = 1 \times 10^6$, when $Q = 2.5 \times 10^5$, the flow pattern exhibits an irregular three-roll structure, accompanied by a flow reversal. When $Q = 6.4 \times 10^5$, the flow displays a relatively regular four-roll structure, with a flow reversal occurring periodically. Conversely, when $Q = 2.25 \times 10^6$, the flow maintains a stable five-roll structure, without any instances of reversal, as shown in figure 1(*d*). Figure 6 illustrates the global angular momentum $L(z)$ corresponding to these three conditions. When $Q = 2.5 \times 10^5$, the global angular momentum $L(z)$ reaches its peaks at $t = 176$ and $t = 221$, respectively, and these peaks are greater than those observed under $Q = 6.4 \times 10^5$. However, as shown in figure 5, the flow does not undergo a rapid reversal after these two peaks, but rather gradually reverses at $t = 230$. In contrast, for $Q = 6.4 \times 10^5$, the flow experiences rapid reversals after the global angular momentum $L(z)$ reaches its peaks at $t = 46$, 102, 160 and 220. It is worth noting that a change in the direction of flow does not necessarily imply a change in the sign of the global angular momentum. The two are not directly related, as both positive and negative global angular momentum can lead to the same result in terms of flow reversal. When $Q = 2.25 \times 10^6$,
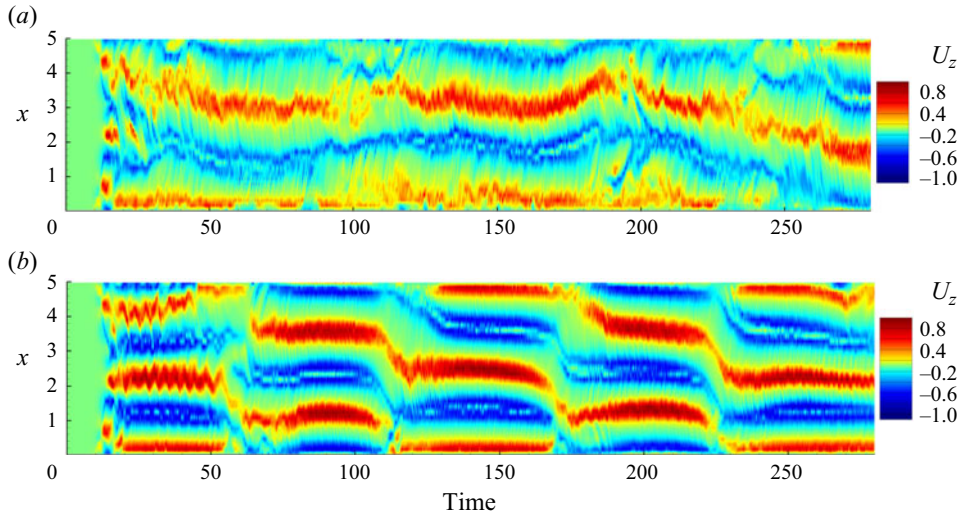
(a)

(b)

Figure 5. Time–space maps of vertical velocity along line $(2.5, y, 0.75)$ for the case with $Ra = 1 \times 10^6$ and (a) $Q = 2.5 \times 10^5$, (b) $Q = 6.4 \times 10^5$.
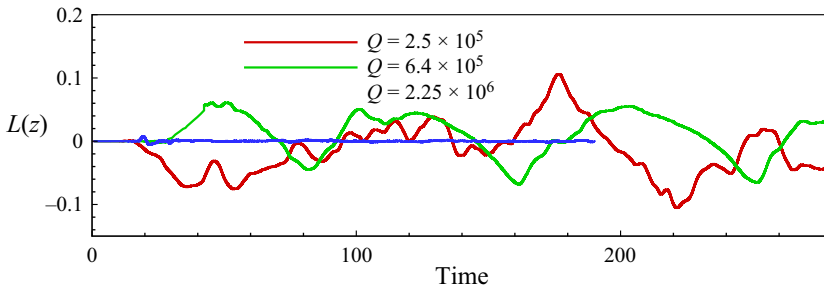

Figure 6. Global angular momentum $L(z)$ along the z direction at the central point of the vessel for three typical flow regimes with $Ra = 1 \times 10^6$ and $Q = 2.5 \times 10^5$, 6.4×10^5, 2.25×10^6.

the flow does not undergo any reversal, resulting in the global angular momentum $L(z)$ almost entirely equalling 0. Therefore, the global angular momentum $L(z)$, which reflects the mean horizontal circulation, can explain to some extent the occurrence of a flow reversal. Additionally, when the magnetic field is weak, the many small-scale, 3-D vortices attached to the primary convective roll contribute to an increase in the global mean horizontal circulation. As a result, $L(z)$ becomes less useful in explaining a flow reversal under these conditions.

In fact, it is not difficult to observe that this periodic reversal bears resemblance to the large-scale temporal intermittency observed in channel flow with a spanwise magnetic field (Boeck *et al.* 2008), forced turbulence in a periodic box (Zikanov & Thess 1998), and inviscid flow in a triaxial ellipsoid (Thess & Zikanov 2007). In these cases, the flows experience prolonged periods of nearly steady laminar states, punctuated by brief turbulent bursts. And the typical duration of the large-scale intermittent cycle is linked intricately to both driving strength and magnetic field intensity. The evolution of all the phenomena also appears to be analogous. When Q is moderate, the magnetic field is not potent enough to suppress 3-D secondary instabilities, but is strong enough to impede their transition to fully developed turbulence. After a brief outburst, the flow reverts to a nearly laminar base state,

980 A24-12

where the Joule dissipation is low, and instabilities can subsist. However, with increasing Q, the strength of the turbulent burst diminishes, and the duration of the instability growth phase extends, resulting in a longer reversal period.

3.3. *Three-dimensionality*

As described above, a horizontal magnetic field of sufficient strength can convert convective motion into quasi-2-D rolls that align parallel to the magnetic field. Additionally, the derivation of the scaling relationship for the cutoff frequency f_c (or cutoff length scale) that distinguishes high-frequency fluctuations in three dimensions from low-frequency fluctuations in two dimensions relies solely on the true interaction parameter Sommeria & Moreau (1982). Hence we expect the scaling law between the interaction parameter and cutoff frequency to apply in the case of turbulent thermal convection influenced by a horizontal magnetic field, as observed in turbulence with a strong background flow (Klein & Pothérat 2010; Pothérat & Klein 2014; Baker *et al.* 2018) and shear turbulence (Chen *et al.* 2021).

Figures 7(*c*–*f*) display pairs of spectra obtained by applying different filter frequencies to the frontal velocity signal. It is noteworthy that, according to the discussion of Kumar & Verma (2018), the Taylor assumption is applicable to turbulent convection. The original signals were collected at positions on the Hartmann walls that aligned precisely with the magnetic field lines (i.e. at $y = 0$ and $y = \Gamma$) but at the same coordinates (x, z), and the probes were located in the central square region to minimize the influence of the sidewalls. Moreover, it should be noted that only the velocity signals recorded by probes positioned in the middle region of adjacent convection rolls are utilized. In the case where $Ra = 10^6$ and $Q = 2 \times 10^5$, the frontal and back spectra are partially identical in figure 7(*c*), which is expected since the flow tends to exhibit quasi-2-D behaviour at most scales. However, the spectra differ significantly at higher frequencies, indicating that small-scale structures are more sensitive to three-dimensionality. As Q decreases (with Ra fixed), the frequency range affected by three-dimensionality extends to lower frequencies, eventually contaminating the entire spectrum at the lowest Q values (e.g. $Q = 0$). By comparing pairs of spectra, the theory of Sommeria & Moreau (1982) and experiments conducted by Baker *et al.* (2018) have identified a cutoff length scale k_c (corresponding to f_c) that separates quasi-2-D structures from 3-D structures.

Here, we applied a partial correlation function between signals on the front and back Hartmann walls (see Pothérat & Klein 2014) to quantify the variation of f_c with N (= Q/Re):

$$c(f) = \frac{\sum_{t=0}^{Ti} \mathscr{B}_f \, u_{front}(t) \, u_{back}(t)}{\sqrt{\sum_{t=0}^{Ti} \mathscr{B}_f \, u_{front}^2(t) \, u_{back}^2(t)}}. \tag{3.20}$$

Here, Ti is the duration of the recorded signals. The signal obtained from the frontal wall is replaced with a filtered counterpart, processed through an eighth-order low-pass filter of cutoff frequency denoted as $\mathscr{B}_f \, u_{front}$, as shown in figure 7(*a*). Generally, the large frequency displayed in the spectrum corresponds to a small flow structure in physical space. As the filter frequency f is increased from 0, more and more fluctuation scales are added to the filtered frontal signal, resulting in better correlation with the back signal in the quasi-2-D flow field. However, when f is increased beyond a critical value f_c (refer to figure 7*f*), the small scales, where three-dimensionality is still present, will disrupt the correlation between the two signals, leading to a decrease in $c(f)$. Hence the position of
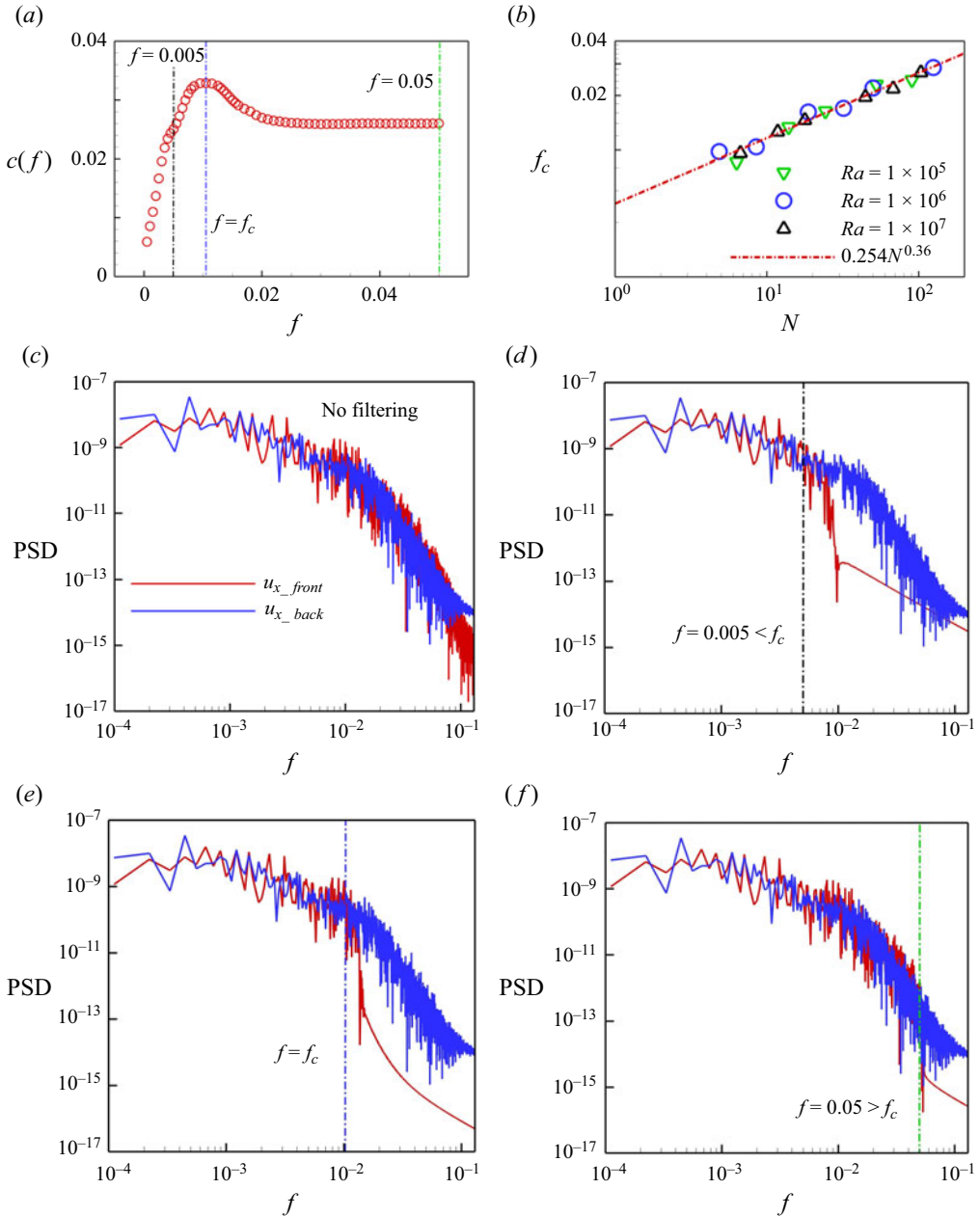
Figure 7. (*a*) Variations of partial correlation $c(f)$ with the cutoff frequency of filter $\mathscr{B}_f$ applied to the velocity signal measured at the frontal wall. Curves are obtained for $Ra = 10^6$ and $Q = 2 \times 10^5$ for a pair of probes within the centre square. Curves obtained for different parameters exhibit the same features. (*b*) The cutoff frequency f_c, separating quasi-2-D large structures from the small 3-D ones with the interaction parameter N. (*c*–*f*) Power spectral density (PSD) of the filtered frontal and back signals plotted in terms of the frequency.

the maximum f_c provides an excellent measure of the separation between large-scale 2-D structure and small-scale 3-D structure.

Figure 7(*b*) depicts the variations of the spatially averaged cutoff frequency f_c with N, indicating that the changes in f_c for all the analysed cases converge onto a single curve. This result implies that f_c follows a scaling law that is determined by N:

$$f_c \sim N^{0.36}. \tag{3.21}$$

This general scaling law provides a precise estimate for the minimum frequency of vortices that are influenced by 3-D inertial effects. Thus, similar to shear turbulence or turbulence with a strong background flow, the MHD-RBC turbulence also exhibits the same scaling law for the cutoff frequency f_c (Klein & Pothérat 2010; Pothérat & Klein 2014; Baker *et al.* 2018).

4. Concluding remarks

The present study reports 3-D DNS of magnetoconvection in a cuboid vessel under the influence of an external horizontal magnetic field. The range of high *Ra* and *Q* never previously explored in numerical simulations is considered.

The results of our DNS are consistent with available experimental and numerical data. In particular, we find a new regime where *Nu* and *Re* reduce with *Q* in flows with weak magnetic fields before the heat transfer enhancement region, demonstrating that this interesting phenomenon is not caused by experimental errors (observed in Burr & Müller 2002; Vogt *et al.* 2021). The similar variation trend in *Nu* and *Re* indicates the strong correlation between heat transfer and momentum transfer. In other words, under a weak magnetic field, the small-scale 3-D vortex structures are inhibited by the Lorentz force, resulting in a decrease in the injection of plumes. These plumes are the main carriers of heat, thus as *Re* decreases, *Nu* decreases accordingly.

As the magnetic field strength increases, the flow gradually reaches a quasi-two-dimensional (quasi-2-D) state. At this point, numerical results show that there is a $-1/3$ scaling relationship between *Re* and *Q*. To better explain this scaling rate, we introduce GL theory into the MHD thermal convection, and use numerical results combined with physical analysis to compare the orders of magnitude of viscous dissipation in the bulk flow region, viscous dissipation within the boundary layer, Joule dissipation in the bulk flow region, and Joule dissipation within the boundary layer, respectively. It is found that under strong magnetic effects, viscous dissipation plays an overwhelmingly dominant role compared to Joule dissipation, and the viscous dissipation within the boundary layer is also much greater than that in the bulk flow region. Therefore, the energy dissipation of the system comes mainly from the viscous dissipation within the boundary layer, i.e. $\varepsilon_\nu + \varepsilon_\eta \sim \varepsilon_\nu \sim \varepsilon_{\nu,BL}$. Combining the heat transfer characteristics under a low *Pr*, we obtain the relationship between heat transfer efficiency and *Re*, and thus derive the $Re \sim Q^{-1/3}$ relationship of the system under strong magnetic fields, which well validates the numerical results.

As for the flow reversal phenomenon observed frequently in liquid metal experiments, we have conducted mechanistic analysis from the method of skewed-varicose instability. For the skewed-varicose instability, the mean horizontal circulation is the most critical influencing factor, which can be measured by the vertical global angular momentum. Our results indicate that the global angular momentum is more suitable for explaining the regular flow reversal phenomenon. For more chaotic flow reversal phenomena, the global angular momentum cannot reflect the evolution process of flow reversal very well.

Indeed, the global angular momentum is greatly influenced by the walls of the container, such as the axial secondary flow caused by the Ekman effect. Therefore, setting the remaining walls, except for the top and bottom plates, as periodic boundaries to observe if the flow reversal phenomenon persists might offer a clearer explanation.

In the meantime, the three-dimensionality is characterized locally by analysing the frequency spectra of the velocity signals near the two Hartmann walls. As predicted by Sommeria & Moreau (1982), the cutoff frequency f_c is in accordance with $\sim N^{0.36}$, indicating the existence of a cutoff frequency that separates 3-D and quasi-2-D turbulent structures in MHD-RBC turbulence, besides the turbulence with a strong background flow (see Baker *et al.* 2018) and shear turbulence (see Chen *et al.* 2021), which corresponds to the cutoff wavelength scaling predicted by Sommeria & Moreau (1982).

Declaration of interests. The authors report no conflict of interest.

Author ORCIDs.
Ming-Jiu Ni https://orcid.org/0000-0003-3699-8370.

REFERENCES

AKHMEDAGAEV, R., ZIKANOV, O., KRASNOV, D. & SCHUMACHER, J. 2020a Rayleigh–Bénard convection in strong vertical magnetic field: flow structure and verification of numerical method. *Magnetohydrodynamics* **56** (2–3), 157–165.

AKHMEDAGAEV, R., ZIKANOV, O., KRASNOV, D. & SCHUMACHER, J. 2020b Turbulent Rayleigh–Bénard convection in a strong vertical magnetic field. *J. Fluid Mech.* **895**, R4.

BAKER, N.T., POTHÉRAT, A., DAVOUST, L. & DEBRAY, F. 2018 Inverse and direct energy cascades in three-dimensional magnetohydrodynamic turbulence at low magnetic Reynolds number. *Phys. Rev. Lett.* **120** (22), 224502.

BOECK, T., KRASNOV, D., THESS, A. & ZIKANOV, O. 2008 Large-scale intermittency of liquid-metal channel flow in a magnetic field. *Phys. Rev. Lett.* **101** (24), 244501.

BURR, U. & MÜLLER, U. 2002 Rayleigh–Bénard convection in liquid metal layers under the influence of a horizontal magnetic field. *J. Fluid Mech.* **453**, 345–369.

BUSSE, F.H. 1978 Non-linear properties of thermal convection. *Rep. Prog. Phys.* **41** (12), 1929.

BUSSE, F.H. & CLEVER, R.M. 1983 Stability of convection rolls in the presence of a horizontal magnetic field. *J. Méc. Théor. Appl.* **2** (4), 495–502.

BUSSE, F.H., KROPP, M. & ZAKS, M. 1992 Spatio-temporal structures in phase-turbulent convection. *Physica* D **61** (1–4), 94–105.

CHAKRABORTY, S. 2008 On scaling laws in turbulent magnetohydrodynamic Rayleigh–Bénard convection. *Physica* D **237** (24), 3233–3236.

CHEN, L., LIU, B.-Q. & NI, M.-J. 2018 Study of natural convection in a heated cavity with magnetic fields normal to the main circulation. *Intl J. Heat Mass Transfer* **127**, 267–277.

CHEN, L., POTHÉRAT, A., NI, M.-J. & MOREAU, R. 2021 Direct numerical simulation of quasi-two-dimensional MHD turbulent shear flows. *J. Fluid Mech.* **915**.

CIONI, S., CHAUMAT, S. & SOMMERIA, J. 2000 Effect of a vertical magnetic field on turbulent Rayleigh–Bénard convection. *Phys. Rev.* E **62** (4), R4520.

DAVIDSON, P.A. 2002 *An Introduction to Magnetohydrodynamics.* Cambridge University Press.

ECKERT, S., GERBETH, G., WITKE, W. & LANGENBRUNNER, H. 2001 MHD turbulence measurements in a sodium channel flow exposed to a transverse magnetic field. *Intl J. Heat Fluid Flow* **22** (3), 358–364.

GREENSIDE, H.S., CROSS, M.C. & COUGHRAN, W.M. JR 1988 Mean flows and the onset of chaos in large-cell convection. *Phys. Rev. Lett.* **60** (22), 2269.

GROSSMANN, S. & LOHSE, D. 2000 Scaling in thermal convection: a unifying theory. *J. Fluid Mech.* **407**, 27–56.

GROSSMANN, S. & LOHSE, D. 2001 Thermal convection for large Prandtl numbers. *Phys. Rev. Lett.* **86** (15), 3316–3319.

HOUCHENS, B.C., WITKOWSKI, L.M. & WALKER, J.S. 2002 Rayleigh–Bénard instability in a vertical cylinder with a vertical magnetic field. *J. Fluid Mech.* **469**, 189–207.

KLEIN, R. & POTHÉRAT, A. 2010 Appearance of three dimensionality in wall-bounded MHD flows. *Phys. Rev. Lett.* **104** (3), 034502.

KRISHNAMURTI, R. & HOWARD, L.N. 1981 Large-scale flow generation in turbulent convection. *Proc. Natl Acad. Sci. USA* **78** (4), 1981–1985.

KUMAR, A. & VERMA, M.K. 2018 Applicability of Taylor's hypothesis in thermally driven turbulence. *R. Soc. Open Sci.* **5** (4), 172152.

LIM, Z.L., CHONG, K.L., DING, G.-Y. & XIA, K.-Q. 2019 Quasistatic magnetoconvection: heat transport enhancement and boundary layer crossing. *J. Fluid Mech.* **870**, 519–542.

LIU, C.Q., WANG, Y.Q., YANG, Y. & DUAN, Z.W. 2016 New omega vortex identification method. *Sci. China Phys. Mech.* **59** (8), 1–9.

LIU, W. 2019 Numerical studies of turbulent Rayleigh–Bénard magnetoconvection in rectangular enclosures. PhD thesis, Technische Universität Ilmenau.

LIU, W., KRASNOV, D. & SCHUMACHER, J. 2018 Wall modes in magnetoconvection at high Hartmann numbers. *J. Fluid Mech.* **849**, R2.

POTHÉRAT, A. & KLEIN, R. 2014 Why, how and when MHD turbulence at low *Rm* becomes three-dimensional. *J. Fluid Mech.* **761**, 168–205.

POTHÉRAT, A. & KLEIN, R. 2017 Do magnetic fields enhance turbulence at low magnetic Reynolds number? *Phys. Rev. Fluids* **2** (6), 063702.

SHRAIMAN, B.I. & SIGGIA, E.D. 1990 Heat transport in high-Rayleigh-number convection. *Phys. Rev.* A **42** (6), 3650.

SOMMERIA, J. & MOREAU, R. 1982 Why, how, and when, MHD turbulence becomes two-dimensional. *J. Fluid Mech.* **118**, 507–518.

SUKORIANSKY, S., ZILBERMAN, I. & BRANOVER, H. 1986 Experimental studies of turbulence in mercury flows with transverse magnetic fields. *Exp. Fluids* **4** (1), 11–16.

TASAKA, Y., IGAKI, K., YANAGISAWA, T., VOGT, T., ZUERNER, T. & ECKERT, S. 2016 Regular flow reversals in Rayleigh–Bénard convection in a horizontal magnetic field. *Phys. Rev.* E **93** (4), 043109.

THESS, A. & ZIKANOV, O. 2007 Transition from two-dimensional to three-dimensional magnetohydrodynamic turbulence. *J. Fluid Mech.* **579**, 383–412.

VOGT, T., ISHIMI, W., YANAGISAWA, T., TASAKA, Y., SAKURABA, A. & ECKERT, S. 2018 Transition between quasi-two-dimensional and three-dimensional Rayleigh–Bénard convection in a horizontal magnetic field. *Phys. Rev. Fluids* **3** (1), 013503.

VOGT, T., YANG, J.-C., SCHINDLER, F. & ECKERT, S. 2021 Free-fall velocities and heat transport enhancement in liquid metal magneto-convection. *J. Fluid Mech.* **915**, A68.

YANAGISAWA, T., HAMANO, Y., MIYAGOSHI, T., YAMAGISHI, Y., TASAKA, Y. & TAKEDA, Y. 2013 Convection patterns in a liquid metal under an imposed horizontal magnetic field. *Phys. Rev.* E **88** (6), 063020.

YANAGISAWA, T., HAMANO, Y. & SAKURABA, A. 2015 Flow reversals in low-Prandtl-number Rayleigh–Bénard convection controlled by horizontal circulations. *Phys. Rev.* E **92** (2), 023018.

YANAGISAWA, T., YAMAGISHI, Y., HAMANO, Y., TASAKA, Y. & TAKEDA, Y. 2011 Spontaneous flow reversals in Rayleigh–Bénard convection of a liquid metal. *Phys. Rev.* E **83** (3), 036307.

YANG, J.C., VOGT, T. & ECKERT, S. 2021 Transition from steady to oscillating convection rolls in Rayleigh–Bénard convection under the influence of a horizontal magnetic field. *Phys. Rev. Fluids* **6** (2), 023502.

ZIKANOV, O., KRASNOV, D., BOECK, T. & SUKORIANSKY, S. 2019 Decay of turbulence in a liquid metal duct flow with transverse magnetic field. *J. Fluid Mech.* **867**, 661–690.

ZIKANOV, O. & THESS, A. 1998 Direct numerical simulation of forced MHD turbulence at low magnetic Reynolds number. *J. Fluid Mech.* **358**, 299–333.

ZUERNER, T., LIU, W., KRASNOV, D. & SCHUMACHER, J. 2016 Heat and momentum transfer for magnetoconvection in a vertical external magnetic field. *Phys. Rev.* E **94** (4), 043108.

ZÜRNER, T. 2020 Refined mean field model of heat and momentum transfer in magnetoconvection. *Phys. Fluids* **32** (10), 107101.